

# Structured generalized sliced Wasserstein distance for keV X-ray polarization analysis with Gas Pixel Detector

Pengcheng Ai<sup>1,2\*</sup>, Hongtao Qin<sup>1,2</sup>, Xiangming Sun<sup>1,2</sup>, Dong Wang<sup>1,2</sup>,  
Huanbo Feng<sup>3</sup>, Hongbang Liu<sup>3</sup>

<sup>1</sup>PLAC, Key Laboratory of Quark and Lepton Physics (MOE), Central China Normal University, No. 152 Luoyu Road, Wuhan, 430079, Hubei, China.

<sup>2</sup>Hubei Provincial Engineering Research Center of Silicon Pixel Chip & Detection Technology, No. 152 Luoyu Road, Wuhan, 430079, Hubei, China.

<sup>3</sup>Guangxi Key Laboratory for Relativistic Astrophysics, School of Physical Science and Technology, Guangxi University, Nanning, 530004, China.

\*Corresponding author(s). E-mail(s): [aipc@ccnu.edu.cn](mailto:aipc@ccnu.edu.cn);

## Abstract

Because of the special angular distribution of excited electrons by the photoelectric effect, the Gas Pixel Detector (GPD) is effective in measuring keV X-ray polarization of astrophysical events (e.g. gamma-ray bursts), by capturing ionization tracks of excited electrons as polarized images. Traditionally, the emission angles of photoelectrons are extracted from polarized images first, and statistics are then performed on these angles to infer the polarization direction and intensity. However, observation with the wide field of view requires the incident angle of X-rays not directly attainable through the traditional analysis process. In this paper, we propose using the generalized sliced Wasserstein (GSW) distance, projected by neural networks with random weights, as a completely data-driven approach to analyze X-ray polarization based on two-dimensional polarized images. We find the structures of the randomized neural networks matter when focusing on different aspects of the polarized images, and take advantage of the discrimination abilities by different neural network structures. The proposed method, named the structured GSW distance, successfully distinguishes polarized images with different configurations of incident angles and polarization directions. Furthermore, we build a simplified statistical model based on the von Mises distribution and the circular Wasserstein distance and compare the model against the proposed method, showing their high consistency. The computational method reported in this paper may benefit GPD-based polarimetry in astroparticle experiments and also pattern analysis on raw data from pixel detectors.

**Keywords:** generalized sliced Wasserstein distance, Gaseous Pixel Detector, X-ray polarization, neural networks

## 1 Introduction

Pixelated detectors have been coupled with ionizable materials because of their distinct advantage to capture spatially extended ionization tracks.

This principle has been adopted in experiments like searching for neutrinoless double-beta decay [1, 2] and dark matter [3], validating the Migdal effect [4], beam monitoring and localization [5],

and measuring X-ray polarization in astroparticle researches [6–8]. The recorded two-dimensional (2D) images have complicated patterns related to rich physical information, making them good candidates for applications of machine learning and neural network techniques [9–12].

In astrophysics, observing gamma-ray bursts (GRBs) provides insights into the formation and evolution of large celestial bodies. Particularly, measuring the polarization of soft X-ray [13] (at keV scale) afterglow is an important probe to GRB properties. Gas Pixel Detectors (GPDs), owing to their superior sensitivity to soft X-rays, were used in commissioned spaceborne experiments (IXPE [6], PolarLight [7], etc.), and will be used in POLAR-2 [8, 14] in the future. In a GPD, the incident X-ray interacts with the working gas through the photoelectric effect, the primary electron ionizes the gas molecules along its track, and ionization charges drift to the charge multiplier under the electric field before detected by the pixel detector. Traditional data analysis involves reconstructing and counting the emission angles of the photoelectrons in individual signal events to match the non-isotropic angular distribution of polarized X-rays.

Although intuitional and well-explainable, the above two-stage process (extracting emission angles and inferring polarization) needs elaborately tuning parameters of the handcrafted algorithm [15] by human experts, and may gradually lose precision in intermediate steps. Besides, for observation with the wide field of view, the analysis is limited to inferring the polarization direction and intensity, while the incident angle of X-rays is of particular interest to physicists to locate the source and facilitate precision measurement. Hence, it is intriguing to devise other ways to utilize the data distribution directly and to fully exploit the physical information lying in the polarized images.

Wasserstein distance [16] is a “distance” to compare two data distributions. The sliced Wasserstein (SW) distance [17] and its generalized variant (GSW) [18] share the statistical properties of the original Wasserstein distance and exhibit as powerful tools to model data distributions in high-dimensional spaces [19, 20]. In the GSW distance, a group of neural networks with randomly initialized weights project the 2D images from the data

space to the feature space where the Wasserstein distance is computed.

In this paper, we propose using the GSW distance as a completely data-driven approach to analyze X-ray polarization based on 2D polarized images. An experimental system with the GPD is constructed to collect data from several configurations of incident angles and polarization directions. Convolutional neural networks with dual-branch structures are empirically designed to effectively distinguish between data distributions and to improve the discrimination power. We name the proposed method the structured generalized sliced Wasserstein (SGSW) distance. It is worth mentioning that the method proposed here is different from conventional deep learning approaches based on supervised learning [21–23], and also different from unsupervised approaches relying on recovering input data [24]. No training is conducted in the process, whether in the supervised way or the unsupervised way.

The rest of the paper is structured as follows: a prototype of the low-energy polarization detector (LPD) at POLAR-2 is introduced in Sect. 2, with a brief description of the data collection for subsequent analysis. The methodology based on the SGSW distance is explained in detail in Sect. 3. The experimental results are given in Sect. 4. A simplified statistical model to evaluate the validity of the results is described in Sect. 5. Finally, Sect. 6 concludes the study.

## 2 Prototype of the POLAR-2/LPD

### 2.1 The detector

POLAR-2 [25] is an international mission with the main goal of observing polarization of GRBs. The LPD [8, 14] of POLAR-2 is individually developed focusing on the energy range of soft X-rays. The main apparatus in LPD is a GPD, with a functional diagram shown in Fig. 1, based on the gas microchannel plate (GMCP) and the Top-metal [26, 27] pixel detector. The X-rays from GRB sources, with the assumed linear polarization, enter the gas chamber and interact with the working gas (mixture of 40% helium and 60% dimethyl ether) through the photoelectric effect. A photoelectron is excited with high probability

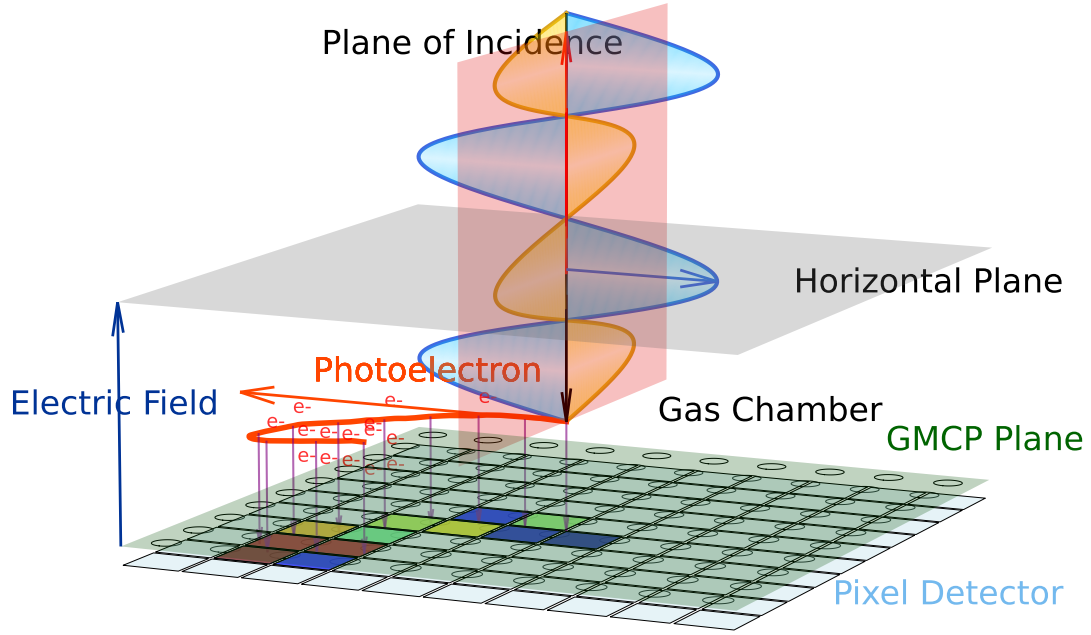


**Fig. 1:** The functional diagram of the GPD based on the gas microchannel plate (GMCP) and the Topmetal pixel detector.

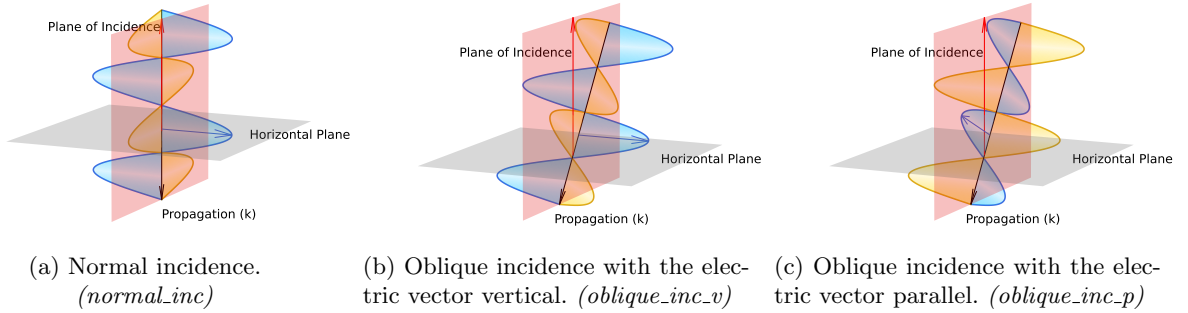


**Fig. 2:** Illustrations of linearly polarized X-rays with different angles of incidences and different directions of electric vectors. The blue shade indicates the electric vector, and the orange shade indicates the magnetic vector.

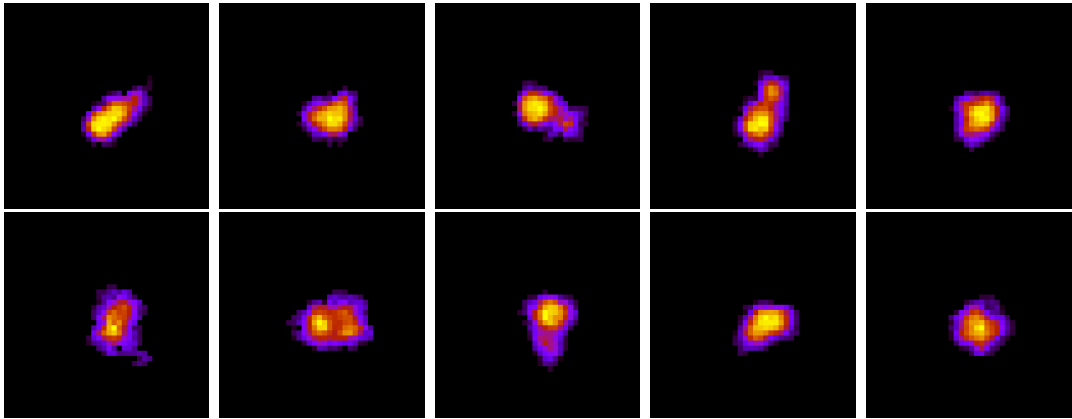
along the direction of the electric vector. Its angular distribution (K-shell, non-relativistic region) is given by [28]:

$$\frac{d\sigma_{\text{ph}}}{d\Omega} \propto \frac{\sin^2 \theta \cos^2 \phi}{(1 - \beta \cos \theta)^4} \quad (1)$$

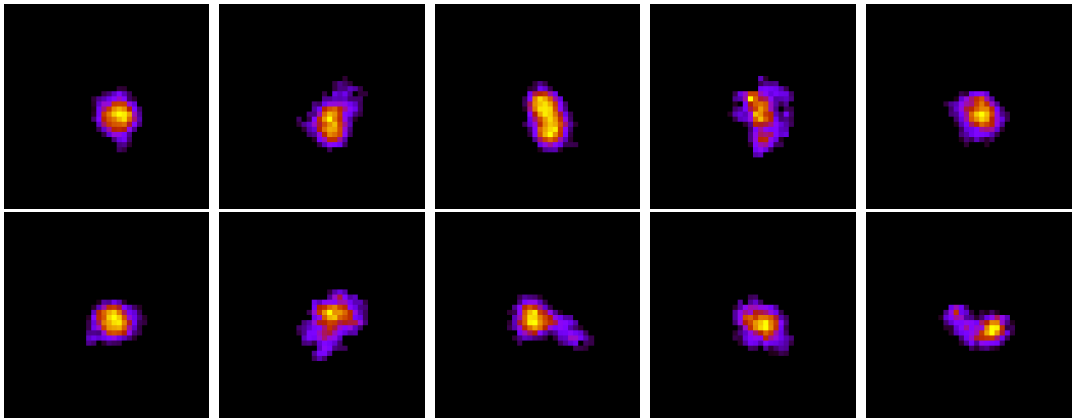
where  $\theta$  is the polar angle relative to the propagation direction,  $\phi$  is the azimuthal angle of the

electric vector, and  $\beta$  is the ratio of the electron speed to the speed of light.

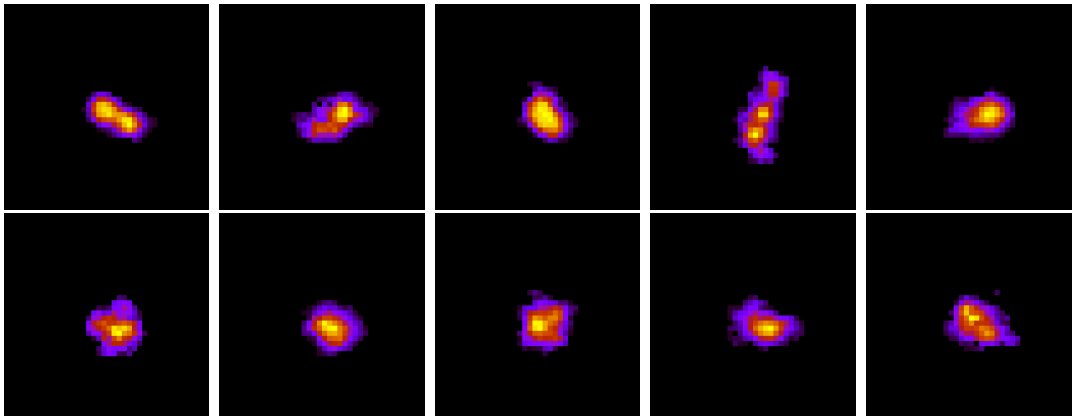
The photoelectron ionizes along its track and forms a Bragg peak at the far end. The ionization charges (electrons) drift under the electric field and multiplies at the GMCP. The Topmetal pixel detector is a direct charge sensor without gas-electron multiplication. The ionization charges are



(a) Normal incidence.



(b) Oblique incidence with the electric vector vertical.



(c) Oblique incidence with the electric vector parallel.

**Fig. 3:** Illustrations of polarized images with different configurations of incident angles and polarization directions. We crop the  $40 \times 40$  area in the center of the pixel detector.

recorded by Topmetal and read out by front-end electronics.

A distinct advantage of POLAR-2/LPD is its wide field of view. Incident X-rays are not limited to a narrow collimator, which improves the detection efficiency but also brings about complexities in data analysis. In Fig. 2, three typical configurations of polarization are illustrated and considered for the rest of the paper: (1) *normal.inc*: the X-ray enters the detector with the propagation direction being normal to the horizontal plane; (2) *oblique.inc.v*: the X-ray enters the detector with oblique incidence, and the electric vector is vertical<sup>1</sup> (perpendicular) to the plane of incidence; and (3) *oblique.inc.p*: the X-ray enters the detector with oblique incidence, and the electric vector is parallel to the plane of incidence. To take into account these configurations, we can acquire and analyze data in real working conditions of POLAR-2/LPD.

## 2.2 Data collection

We construct a data collection platform [29] for calibration of POLAR-2/LPD with linearly polarized X-ray sources at the energy of 4.51 keV. The polarized images from the Topmetal pixel detector are triggered and filtered before passed to storage. Some exemplary images, with three different configurations discussed above, are shown in Fig. 3. By carefully examining the images, we can find some notable characteristics:

- Almost all images exhibit strong signal features, with a spacially extended track and a bright Bragg peak at one end of the track.
- There is a considerable amount of images, however, leaving tracks in a relatively confined region and showing very subtle directional hints. These images contribute to the randomness in the reconstruction of angular distribution.
- Compared to the images with normal incidence, images with oblique incidence display more complicated features, with more dispersed and atypical examples.

In general, images show correspondence to major characteristics of the theoretical angular distribution. Extracting the emission angle of the

<sup>1</sup>We use the term “vertical” for X-rays with the electric vector perpendicular to the plane of incidence to avoid confusion with “parallel” in the abbreviation.

photoelectron can be a challenging task for human experts with direct observations. Besides, it can be difficult to differentiate between configurations with varied incident angles and polarization directions. This makes the data-driven approach appealing in this high-dimensional data analysis task.

## 3 Methodology

**Table 1:** Details of the neural network architecture of the baseline model.

Part	Name	Kernel Size	Output Size
(Input)	–	–	40×40×1
Backbone	Conv.1 <sup>1</sup>	3×3×1×32 <sup>2</sup>	40×40×32
	Conv.2 <sup>1</sup>	3×3×32×32 <sup>2</sup>	40×40×32
Branch-s <sup>3</sup>	Pool	–	1×1×32
	Flatten	–	32
	Dense	32×1 <sup>2</sup>	1
Branch-l <sup>3</sup>	Pool	–	8×8×32
	Flatten	–	2048
	Dense	2048×1 <sup>2</sup>	1

<sup>1</sup>The Rectified Linear Units (ReLU) follow each of these layers.

<sup>2</sup>Here we list the kernel size of weights, the size of biases is equal to the last dimension of the kernel size.

<sup>3</sup>These two branches share the backbone.

For application of the proposed method, we preprocess the input data for better feature extraction. The original image size is 100×100, we crop it to 40×40 to exclude unfired surrounding pixels. Cropped images are shifted in sub-pixel resolution to locate the center of mass in the middle of the image<sup>2</sup>. An optional rotation operation is performed before or after the cropping and center-of-mass aligning to study the images with particular polarization directions. Finally, the image is normalized to subtract the mean intensity and to be divided by the standard deviation of the intensity.

To apply the SGSW distance, we construct the architecture of individual neural networks, illustrated in Fig. 4. The architecture itself is a convolutional neural network commonly found in

<sup>2</sup>For branch-s of the neural network, center-of-mass aligning can be omitted because this branch is shift-invariant.

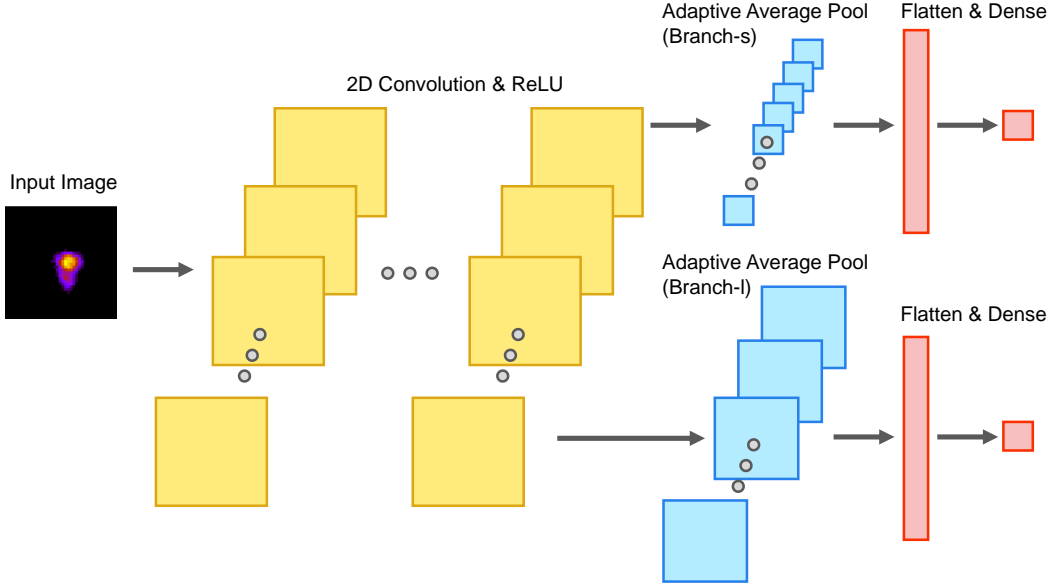


**Fig. 4:** The architecture of individual neural networks for the structured generalized sliced Wasserstein (SGSW) distance. The architecture is composed of 2D convolution, ReLU activation function, adaptive average pooling and dense connections. Choosing different pooling sizes in adaptive average pooling results in different sizes of feature maps before flattening.

computer vision tasks [30]. What we modify here is the adaptive average pooling to generate outputs with a dual-branch structure: we reduce the feature map to different sizes by this adaptive layer to focus on different scales on the original input data. The two branches assist each other to improve the discrimination power in the generated predictive values after dense connections (see Sect. 4.1).

With this architecture, we create a baseline model as our initial attempt for multi-scale feature extraction. The details of the baseline model are given in Table 1. We use two convolution layers as our backbone, with the Rectified Linear Unit (ReLU) as the activation function. We add zero paddings at the boundary of the feature map to keep its size unchanged after convolution. For branch-s, adaptive average pooling reduces the size of feature map to  $1 \times 1$  while keeping the channel dimension (32). A densely connected layer further transforms the size to unity after it is flattened. For branch-l, adaptive average pooling reduces the size of feature map to  $8 \times 8$ . Then, it is flattened to 2048, and transformed to unity by dense connections.

It can be seen that the neural network architecture used here is very lightweight. The number of parameters is just about 11.65k, which is much less than state-of-the-art neural network models. For the GSW distance, models with complicated architectures are not always advantageous for improving discrimination power, because high level features are hard to exploit by deep structures with random weights (see Sect. 4.2 for more discussions).

At initialization, an ensemble of neural networks (64 in this paper) with the same architecture is initialized with random weights and biases. We use the initialization method proposed in [31] (as default by PyTorch [32] deep learning framework):

$$W, b \sim \mathcal{U}\left(-\frac{1}{\sqrt{D}}, \frac{1}{\sqrt{D}}\right) \quad (2)$$

where:

$$D = C_{\text{in}} \times K_{\text{height}} \times K_{\text{width}} \quad (3)$$

for convolution layers, and

$$D = L_{\text{in}} \quad (4)$$

for linear (densely connected) layers. In equation (2),  $\mathcal{U}(\cdot, \cdot)$  denotes the uniform distribution. In equation (3),  $C_{\text{in}}$  denotes the input channel size and  $K_{\text{height/width}}$  denotes the kernel size. In equation (4),  $L_{\text{in}}$  denotes the input feature length. To ensure neural networks are initialized to various parameters and to ease reproducing the results, we use a series of predefined random seeds for each neural network when initialization.

To compute the GSW distance for each branch, we randomly select two batches of examples from two datasets. These two datasets can be polarized images with different configurations, or with different polarization directions achieved by rotation. Suppose we get two batches of data ( $\mathbf{B}_1^{(1:N)}$ ,  $\mathbf{B}_2^{(1:N)}$ ) with shape (batch size, image height, image width), the one-dimensional Wasserstein distance is given by:

$$\mathbf{Y}_{1,i}^{(1:N)} = \text{Model}_i(\mathbf{B}_1^{(1:N)}) \quad i = 1, 2, \dots, M \quad (5)$$

$$\mathbf{Y}_{2,i}^{(1:N)} = \text{Model}_i(\mathbf{B}_2^{(1:N)}) \quad i = 1, 2, \dots, M \quad (6)$$

$$W = \frac{1}{MN} \sum_{i=1}^M \sum_{j=1}^N \left| \text{Sort}(\mathbf{Y}_{1,i})^{(j)} - \text{Sort}(\mathbf{Y}_{2,i})^{(j)} \right| \quad (7)$$

where  $M$  represents the number of neural networks in the ensemble,  $N$  represents the number of examples in a batch (batch size),  $\text{Model}_i(\cdot)$  represents the inference model of each neural network,  $\text{Sort}(\cdot)$  represents the sorting operation applied to a series of numbers, and  $W$  represents the computed Wasserstein distance. It can be seen in the following sections that, although each neural network is simple and completely random, the ensemble of neural networks works as a universal feature extractor and gives meaningful distances across datasets, paving the way for effective discrimination.

## 4 Results

We conduct experiments based on the datasets collected by the GPD and the method described above. The datasets include three configurations, in which 168631 examples are for normal incidence (*normal\_inc*), 93856 examples for oblique incidence with the electric vector vertical to the plane of incidence (*oblique\_inc\_v*), and 55834 examples

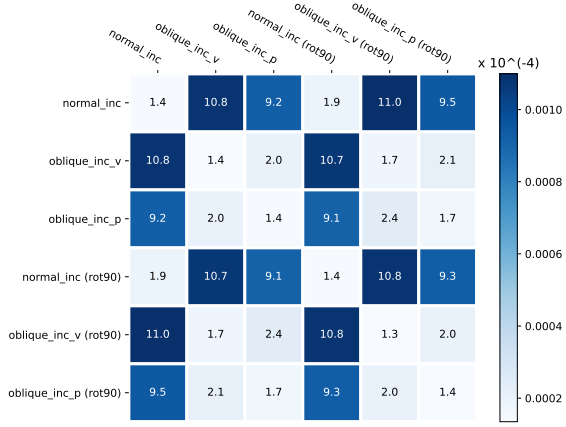
for oblique incidence with the electric vector parallel to the plane of incidence (*oblique\_inc\_p*). Examples are randomly selected from the datasets to form batches. For oblique incidence, the angle between the propagation direction and the plane of incidence is 30 degrees. The ensemble of neural networks is implemented using the PyTorch [32] deep learning framework, with 64 individuals in the ensemble. We use graphic processing units (NVIDIA GeForce RTX 4060Ti 16GB) to accelerate the inference of neural networks. We use the baseline model, with batch size of 512, to generate the main results. To improve the statistical significance, we compute the mean and standard deviation based on the results of 100 batches.

### 4.1 Main results

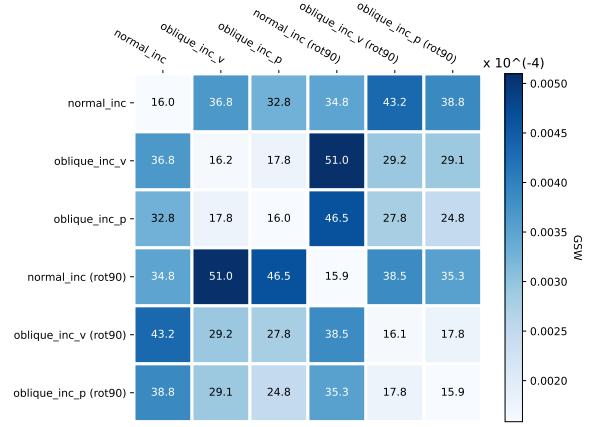
Firstly, we evaluate the overall performance of the proposed method using a matrix of GSW distances across several conditions. The matrices showing the original GSW distances are plotted in Fig. 5, where Fig. 5a is for the branch-s of the baseline model and Fig. 5b is for the branch-l of the baseline model. In total, six conditions are considered: *normal\_inc*, *oblique\_inc\_v*, *oblique\_inc\_p*, and their variations by 90-degree rotation. The diagonal elements indicate the GSW distances within the same condition, and the non-diagonal elements indicate the GSW distances between different conditions. The numbers in the squares indicate the computed GSW distances.

Compared to the confusion matrix which prefers large values for diagonal elements, the matrix of GSW distances here prefers small values for diagonal elements and large values for non-diagonal elements. It can be seen in Fig. 5 that all diagonal elements take the smallest values in their rows and columns, which conforms to the statistical meaning of GSW distances being a measure of data distributions. Besides, the contrast ratio between the non-diagonal element and the corresponding diagonal element indicate the discrimination power of the GSW distance. It can be seen that these two branches have distinct characteristics in discrimination power, indicated by different color patterns.

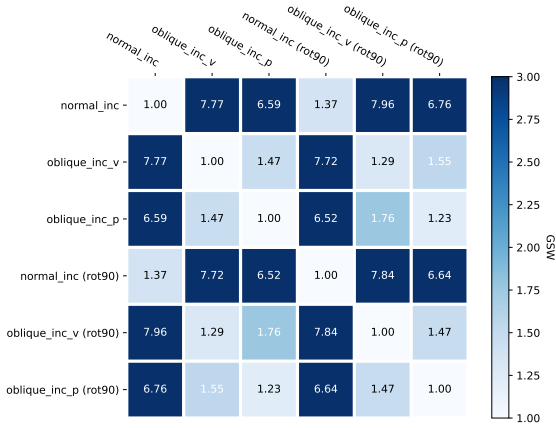
The values of GSW distances are on the order of  $1 \times 10^{-4}$  for branch-s and  $10 \times 10^{-4}$  for branch-l. To more comprehensively evaluate the two branches, we unify the matrices by their diagonal



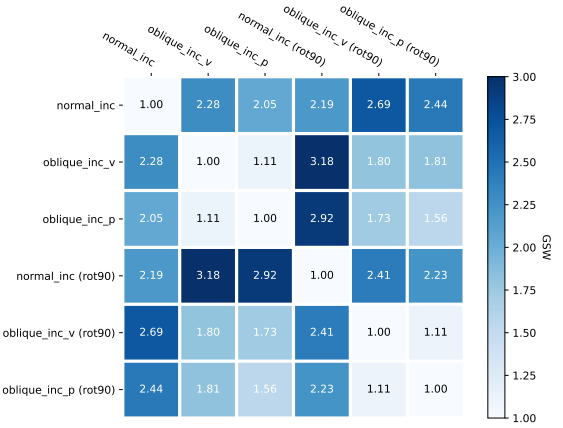
(a) Matrix of branch-s.



(b) Matrix of branch-l.

**Fig. 5:** Matrices showing the original GSW distances of two branches across different configurations and rotations.

(a) Matrix of branch-s.



(b) Matrix of branch-l.

**Fig. 6:** Matrices showing the unified GSW distances of two branches across different configurations and rotations. The color bar is for the range from 1.00 to 3.00, and values larger than 3.00 are plotted using the darkest color.

elements:

$$\mathbf{G} = \text{diag}\left(\frac{1}{\sqrt{a_{11}}}, \frac{1}{\sqrt{a_{22}}}, \dots, \frac{1}{\sqrt{a_{66}}}\right) \quad (8)$$

$$\hat{\mathbf{A}} = \mathbf{G}\mathbf{A}\mathbf{G} \quad (9)$$

where  $\mathbf{A}$  and  $a_{ij}$  denote the original matrix and its element,  $\mathbf{G}$  denotes a diagonal matrix, and  $\hat{\mathbf{A}}$  denotes the unified matrix. After unification, the relative intensity on the matrix is kept as

the same, and all diagonal elements are rendered values of unity. The matrices showing the unified GSW distances are displayed in Fig. 6. From this figure, it can be seen more clearly the strength in discrimination power of each branch. For branch-s, it can be more definitely discriminated between different configurations (*normal\_inc* vs. *oblique\_inc\_v*, etc.), and less definitely discriminated between rotations (*normal\_inc* vs. *normal\_inc (rot90)*, etc.). On the contrary, for

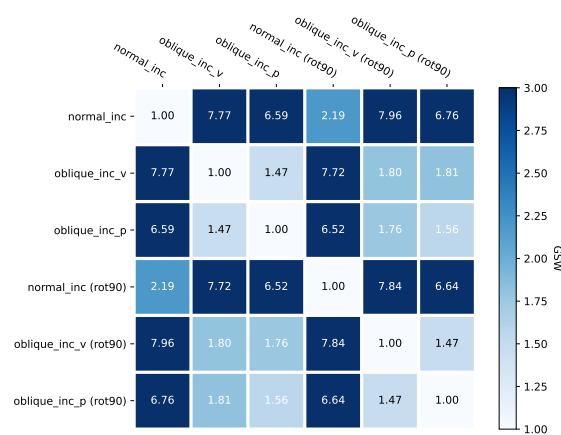


**Fig. 7:** The matrix showing the combined unified GSW distances (SGSW distances) of the two branches.

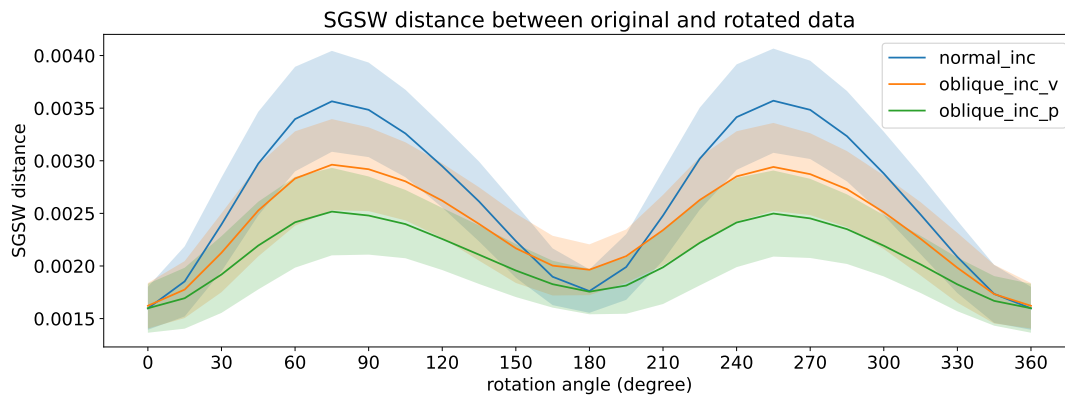


**Fig. 8:** The curves of the SGSW distances between the distribution of original images and the distributions of images after rotation.

branch-1, it becomes a strength in discrimination between rotations rather than between configurations. Hence, the two branches can work in conditions complementary to each other and jointly improve the discrimination power across configurations and rotations.

To physically interpret the results, we review the neural network architecture of the baseline model. For branch-s, the adaptive average pooling reduces the size of feature map to  $1 \times 1$ . As a result, it focuses on the overall characteristics of the input images but loses most spatially extended information. In our physical context, it can discriminate better between different configurations of incident angles and polarization directions than between rotations of polarized images. For branch-l, the adaptive average pooling reduces the size

of feature map to  $8 \times 8$ , so it still keeps the spatially extended information, making it a good discriminator for rotations of polarized images.

In Fig. 7, we combine the two unified matrices by taking the larger value in each element:

$$\tilde{a}_{ij} = \max(\hat{a}_{ij}^s, \hat{a}_{ij}^l) \quad (10)$$

where  $\tilde{a}_{ij}$  denotes the element of the combined matrix ( $\tilde{\mathbf{A}}$ ),  $\hat{a}_{ij}^s$  denotes the element from the unified matrix of branch-s ( $\hat{\mathbf{A}}^s$ ), and  $\hat{a}_{ij}^l$  denotes the element from the unified matrix of branch-l ( $\hat{\mathbf{A}}^l$ ). The elements in  $\tilde{\mathbf{A}}$  represent the comprehensive discrimination ability of the proposed SGSW distance. When performing polarization analysis, however, one should choose a particular aspect

for discrimination (configuration or rotation) and trace back to a certain branch.

In analysis of dynamics of polarized lights, it is meaningful to acquire the azimuthal angle of polarization, or the direction of the electric vector, from the angular distribution of photoelectrons. To study the relation between the SGSW distance and the azimuthal angle, we rotate the polarized images in each configuration and compute the SGSW distance between the distributions of original images and the rotated images. The results are gathered as curves in Fig. 8. Three configurations (*normal\_inc*, *oblique\_inc\_v*, *oblique\_inc\_p*) are plotted in separate colors from 0 degree to 360 degrees with a step of 15 degrees, and the error bands indicate the standard deviations.

It can be seen in this figure that all three curves show the correct correspondence to the angular distribution in equation (1). The highest probability lies in 0 degree and 180 degrees in the angular distribution, and the lowest probability lies in 90 degrees and 270 degrees. When rotating through 90 degrees or 270 degrees, the locations of lowest probabilities in the distribution of rotated images coincide with the locations of highest probabilities in the distribution of original images, which gives peaks in the curve of SGSW distances. When rotating through 180 degrees or 360 degrees, the locations of lowest probabilities and highest probabilities do not change, which gives valleys in the curve of SGSW distances. Although not perfectly aligning with the theoretically analysis, the curves have similar trends and distinct peaks and valleys. Besides, the configuration *normal\_inc* has the highest peak-to-valley ratio, with the configuration *oblique\_inc\_v* being the second and the configuration *oblique\_inc\_p* being the third. An explanation of this phenomenon by a simplified statistical model is given in Sect. 5.

Finally, it is interesting to compare the curves in Fig. 8 with the modulation curves in literature (4.5 keV X-rays in [8]). The modulation curve directly reflects the angular distribution of excited photoelectrons. The modulation factor reported in [8] is 41.28%. Using the same equation, the equivalent modulation factor in Fig. 8 for the configuration *normal\_inc* is 38.18%, which is close to the real modulation factor. Nevertheless, it is worth mentioning that, although these two kinds of curves have similar shapes, they are

two things with totally different physical meanings, and the experimental conditions are not the same, so the results may not be fully comparable<sup>3</sup>. Besides, the method proposed here has the potential to discriminate images from nonidentical configurations, while modulation curves cannot.

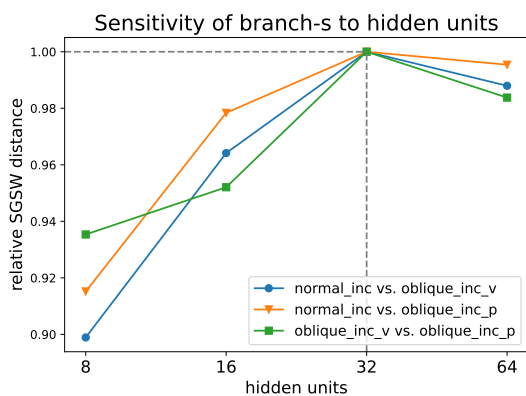
## 4.2 Analysis of sensitivity

To investigate the influence of changing neural network architectures and number of examples in the distribution, we perform a sensitivity analysis on hyperparameters of the neural network and the batch size. The results are gathered in Fig. 9. For branch-s, we conduct experiments between different configurations. For branch-l, we conduct experiments between each configuration and its rotated variation. All results are unified and relative to the baseline model. The discussions of the results are presented as follows:

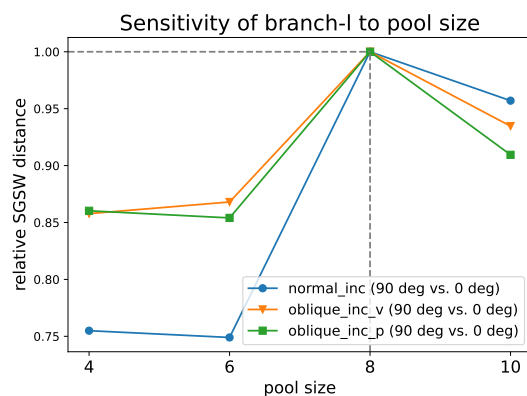
- In Fig. 9a, we investigate the impact of hidden units on the discrimination performance of branch-s. We find that, increasing the number of hidden units initially improves the the discrimination performance (from 8 to 32), but when hidden units reach a certain value, the performance begins to shrink. It indicates that there is an optimal choice of hidden units to restrict the complexity of the neural network.
- In Fig. 9b, we investigate how the size of adaptive average pooling impacts the discrimination performance of branch-l. When the pool size is small (below 6), the performance is limited. When the pool size increases to a certain amount, the performance is boosted, but begins to shrink when increased further. It indicates the reasonable choice of the pool size is important for discrimination performance of branch-l.
- In Fig. 9c and Fig. 9d, we investigate the impact of hidden convolution layers on the discrimination power. For branch-s, fewer layers are more preferable to improve the performance. However, for branch-l, a large gap exists between one hidden layer and two or more hidden layers. It indicates, while branch-s can better discriminate on shallow features, branch-l needs the deep structure to reach the ideal performance.

---

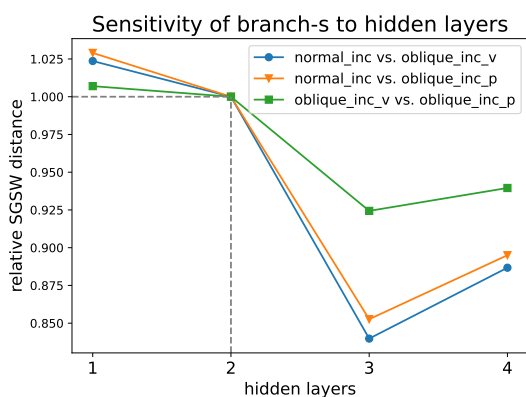
<sup>3</sup>We will see in Sect. 4.2 that increasing the batch size will improve the equivalent modulation factor.



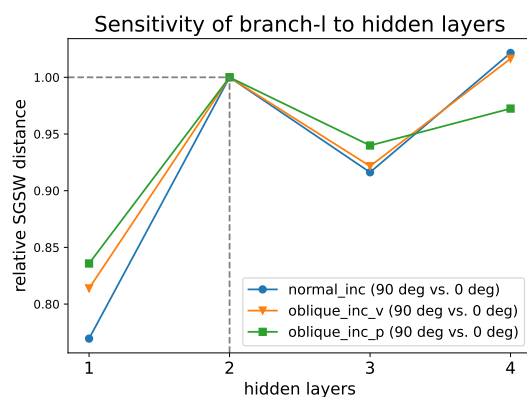
(a) Hidden units for branch-s.



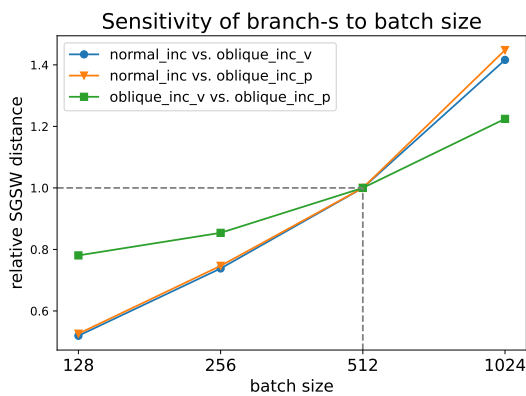
(b) Pool size for branch-l.



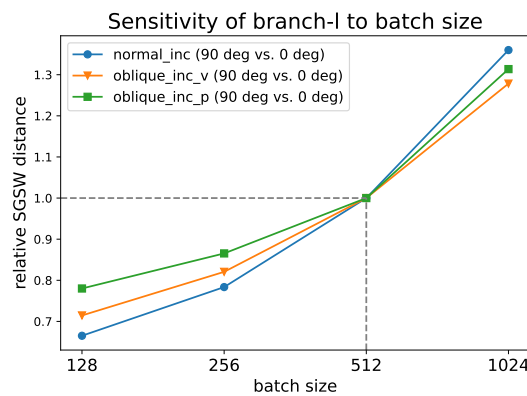
(c) Layers for branch-s.



(d) Layers for branch-l.



(e) Batch size for branch-s.



(f) Batch size for branch-l.

**Fig. 9:** Line plots showing the sensitivity of two branches to hyperparameters of the neural network and the batch size. We use the baseline model as the reference when comparing different values of variables.

- In Fig. 9e and Fig. 9f, we investigate the impact of the batch size on the discrimination power. It can be seen that, the performance of two branches increases monotonically with the batch size. This result is reasonable considering the data distribution of polarized images with a substantial amount showing subtle directional hints. More examples will illustrate the distributional profile more accurately, and thus give larger SGSW distances.

## 5 Statistical model

In this section, we demonstrate the validity of results between original and rotated images through a simplified statistical model. Apart from geometric transformations, we make one core assumption that the detected emission angle of the photoelectron obeys the von Mises distribution [33] centering the real emission angle. Under this assumption, we can calculate the circular Wasserstein (CW) distance [34] between two angular distributions. The choices of the von Mises distribution and the CW distance are based on the fact that we perform statistics on a circular plane.

The algorithmic procedure of computing the CW distance on the statistical model is shown in Algorithm 1. In this algorithm, the function `SINGLESAMPLE` produces a unit vector in the space rectangular coordinate system from polar and azimuthal angles, and performs an additional rotation around the y-axis. The function `BATCHSAMPLE` produces a collection of detected emission angles. Firstly, the polar and azimuthal angles are sampled from a squared-sine distribution according to equation (1) (the relativistic effect is not considered for simplicity, and the default direction of the electric vector is along the y-axis). Then we sample a unit vector using the aforementioned function with additional rotation and adjustment to the azimuthal angle to simulate different configurations. Afterwards, the direction on the x-y plane is determined by the unit vector, and an angle is sampled from the von Mises distribution, with a predefined kappa coefficient, centering the direction on the x-y plane. Finally, this sampled angle is added to the collection. We repeat the sampling loop until we get enough examples to form a sufficient angular distribution.

When computing the CW distance, we follow the procedure `COMPUTE_CW`. Two batches

are sampled with independent configurations and rotations. The  $\theta_{i,*}$ ,  $\phi_{i,*}$ ,  $\alpha_{i,*}$  correspond to the angle of inclination for oblique incidence, the direction of the electric vector, and the rotation angle, respectively. Then the circular Wasserstein distance is computed on the two batches.

When implementing the algorithm, we use SciPy [35] and POT [36] libraries in Python for the von Mises distribution sampling and CW distance computation. We use the batch size of 512, and compute the mean and the standard deviation on 64 batches. The results for three configurations on different rotation angles are shown in Fig. 10. The only tunable parameter for the algorithm is the kappa coefficient for the von Mises distribution. We manually adjust kappa (which is set to 1.85 in the model) to match the amplitudes proportionally between the experimental results and the statistical model. By comparing this figure and Fig. 8, we can find that they share many similarities. The shapes of the curves are very alike, the peaks for three configurations (*normal\_inc*, *oblique\_inc\_v*, *oblique\_inc\_p*) have the same ordering, and the shades indicating the standard deviations are on the same scale.

To numerically compare the two figures, we calculate the peak-to-valley ratio and the average standard deviation to mean for three configurations with two kinds of Wasserstein distances. The results are shown in Table 2. It can be seen that the two separate analysis procedures have very similar quantities. Among the configurations, *normal\_inc* and *oblique\_inc\_v* can match very closely, while the statistical model slightly overestimates the quantities for *oblique\_inc\_p*. In summary, it is demonstrated that a statistical model with simple assumptions can very well fit the experimental results.

## 6 Conclusions and outlook

In this paper, we present a data-driven approach for GPD-based polarization analysis on direct charge images in astroparticle experiments. A prototype of the LPD in the POLAR-2 experiment is constructed for researching soft X-rays on the keV scale. Images from three configurations with varied incident angles and polarization directions are

---

**Algorithm 1** Calculate the circular Wasserstein distance with the statistical model

---

**Require:**  $\kappa$ : kappa coefficient for the von Mises distribution;  $B$ : batch size.

**Ensure:**  $\kappa > 0$ .

```

1: function SINGLESAMPLE( $\theta, \phi, \gamma$ )
2:    $\mathbf{V} \leftarrow (\sin(\theta) \cos(\phi), \sin(\theta) \sin(\phi), \cos(\theta))^T$ 
3:   Rotate  $\mathbf{V}$  around rotational axis  $(0, 1, 0)^T$  by angle  $\gamma$ 
4:   return  $\mathbf{V}$ 
5: end function
6:
7: function BATCHSAMPLE( $\theta_i, \phi_i, \alpha_i$ )
8:    $\Omega_\beta \leftarrow \emptyset, n \leftarrow 0$ 
9:   while  $n < B$  do
10:    Sample  $\theta_o, \phi_o \sim p(\theta, \phi) = \frac{\sin^2(\theta) \sin^2(\phi)}{\pi^2}, \theta, \phi \in [0, 2\pi)$ 
11:     $\mathbf{V}_n \leftarrow \text{SINGLESAMPLE}(\theta_o, \phi_o + \phi_i, \theta_i)$ 
12:     $\alpha_o \leftarrow \arctan 2(V_{n,y}, V_{n,x})$ 
13:    Sample  $\beta \sim \text{VONMISES}(\kappa, \alpha_o + \alpha_i)$ 
14:     $\Omega_\beta \leftarrow \Omega_\beta \cup \{\beta\}$ 
15:     $n \leftarrow n + 1$ 
16:   end while
17:   return  $\Omega_\beta$ 
18: end function
19:
20: procedure COMPUTECW( $\theta_{i,1}, \phi_{i,1}, \alpha_{i,1}, \theta_{i,2}, \phi_{i,2}, \alpha_{i,2}$ )
21:    $\Omega_{\beta,1} \leftarrow \text{BATCHSAMPLE}(\theta_{i,1}, \phi_{i,1}, \alpha_{i,1})$ 
22:    $\Omega_{\beta,2} \leftarrow \text{BATCHSAMPLE}(\theta_{i,2}, \phi_{i,2}, \alpha_{i,2})$ 
23:    $W \leftarrow \text{CIRCULARWASSERSTEIN}(\Omega_{\beta,1}, \Omega_{\beta,2})$ 
24: end procedure

```

---

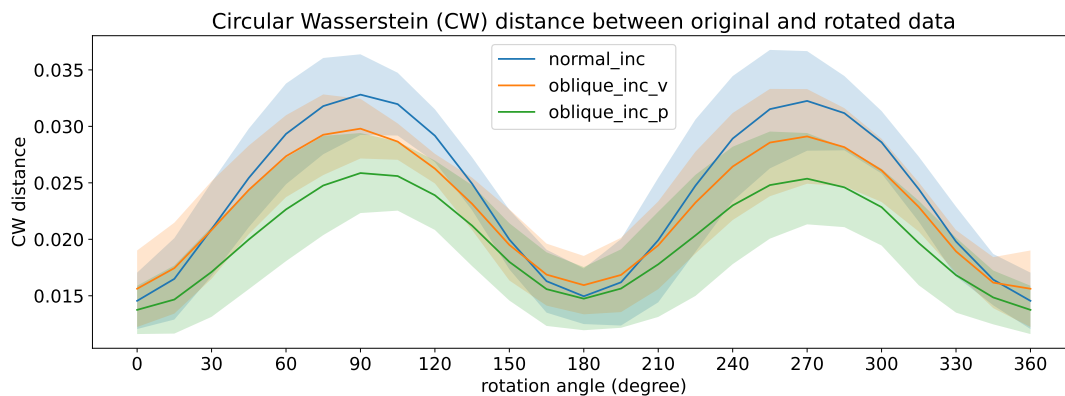


**Fig. 10:** The curves of the circular Wasserstein distances on the statistical model between the distribution of original angular samples and the distributions of angular samples after rotation.

collected on the platform of the detector prototype. Initial observation reveals the subtle distinctions between the image patterns from different configurations.

The major contribution of the paper is a method to compare the data distributions of two image sets through the SGSW distance, using an ensemble of neural networks with randomly

**Table 2:** Comparison on the peak-to-valley ratio and the average standard deviation (std.) to mean between the SGSW distances from the experiments and the CW distances from the statistical model.

Configuration	Peak-to-valley ratio		Average std. to mean	
	Experimental	Statistical Model	Experimental	Statistical Model
<i>normal_inc</i>	2.2352	2.2548	0.1469	0.1566
<i>oblique_inc_v</i>	1.8267	1.9073	0.1456	0.1485
<i>oblique_inc_p</i>	1.5747	1.8810	0.1519	0.1863

initialized weights. This method is applied to analyzing the polarized images from GPD to reveal the mismatches in angular distributions of photoelectrons. Unlike conventional supervised or unsupervised approaches, the proposed method does not depend on explicit training or optimization, making it a good candidate for raw experimental data without labelling by extra equipments or modelling in simulation.

In experiments, we evaluate the SGSW distance on image data from several configurations and also azimuthal rotations. The results show that the proposed distance measure has the ability to distinguish between different image patterns and angular distributions. What we find empirically is that the dual-branch structures of the neural network work in a complementary manner, with each branch focusing on distinct aspects of the data distribution. These results can be a first step towards discriminative analysis with more sophisticated neural network architectures, paving the way for future researches.

Finally, we build a simplified statistical model to demonstrate the validity of the experimental results. The statistical model is based on the von Mises distribution and the CW distance. We give an algorithmic procedure to implement the statistical model and to compute the CW distance systematically. The results from the statistical model show high consistency with results from the experiments, which cross-validates the credibility from physical and statistical perspectives.

The method and results reported here have extensive implications. For GPD-based astroparticle experiments, this method can be an effective toolchain to assist polarization analysis prior to conventional feature extraction. In particular, for POLAR-2/LPD, the wide field of view necessitates analytical measures to acquire additional information from incident signal events and to

facilitate precision measurement of X-ray polarization.

Apart from applications in astroparticle physics, the method can also be employed in any circumstances where there are abundant image data. For example, the SGSW distance can be used for anomaly detection and searching for new physics in high energy physics experiments [24]. Besides, it can be used in generative models to evaluate the quality of generation and to mitigate the gap between simulation to reality [37, 38]. It is worth mentioning that the applications are not limited to 2D spaces. As a matter of course, it works naturally with one-dimensional or three-dimensional data.

Future work includes investigating the proposed method in more application scenarios, enhancing the discrimination power with dedicated neural network architectures, and improving the robustness of the method when it is used with fewer examples and more complex data distributions. We sincerely hope the method proposed here will benefit researchers and practitioners in this area as an effective computational tool for more real-world experiments.

**Acknowledgements.** This research is supported by the National Natural Science Foundation of China (Grant Nos. 12405228, U1731239, 12027803, 12133003), the National Key Research and Development Program of China (Grant Nos. 2024YFF0726201, 2024YFA1611700), the China Postdoctoral Science Foundation (Grant No. 2023M731244), the special funding for Guangxi Bagui Scholars, the Guangxi Key Research and Development Program (Guike FN2504240040), the Guangxi Talent Program ("Highland of Innovation Talents"), and the Innovation Project of Guangxi Graduate Education (No. YCBZ2025045).

**Data Availability Statement.** This manuscript has no associated data or the data will not be deposited. [Authors' comment: The data can be made available upon reasonable request from Huanbo Feng.]

**Code Availability Statement.** Code/software will be made available on reasonable request. [Authors' comment: The code/software generated and/or analyzed during the current study can be made available upon reasonable request from the corresponding author.]

## References

- [1] Wang, J., Wang, H., Zhang, D.: Solar neutrino background in high-pressure gaseous  $^{82}\text{SeF}_6$  TPC neutrinoless double beta decay experiments. *Chinese Physics C* **48**(4), 043003 (2024) <https://doi.org/10.1088/1674-1137/ad2675>
- [2] Filipenko, M., Gleixner, T., Anton, G., Durst, J., Michel, T.: Characterization of the energy resolution and the tracking capabilities of a hybrid pixel detector with CdTe-sensor layer for a possible use in a neutrinoless double beta decay experiment. *The European Physical Journal C* **73**(4), 2374 (2013) <https://doi.org/10.1140/epjc/s10052-013-2374-1>
- [3] Amaro, F.D., et al.: The CYGNO Experiment. *Instruments* **6**(1) (2022) <https://doi.org/10.3390/instruments6010006>
- [4] Yi, D., et al.: Direct observation of the Migdal effect induced by neutron bombardment. *Nature* **649**(8097), 580–583 (2026) <https://doi.org/10.1038/s41586-025-09918-8>
- [5] Wang, H.-L., et al.: Design and tests of the prototype beam monitor of the CSR external target experiment. *Nuclear Science and Techniques* **33**(3), 36 (2022) <https://doi.org/10.1007/s41365-022-01021-1>
- [6] Weisskopf, M.C., et al.: The Imaging X-ray Polarimetry Explorer (IXPE). *Results in Physics* **6**, 1179–1180 (2016) <https://doi.org/10.1016/j.rinp.2016.10.021>
- [7] Feng, H., et al.: PolarLight: a CubeSat X-ray polarimeter based on the gas pixel detector. *Experimental Astronomy* **47**(1), 225–243 (2019) <https://doi.org/10.1007/s10686-019-09625-z>
- [8] Feng, H.-B., et al.: Gas microchannel plate-pixel detector for X-ray polarimetry. *Nuclear Science and Techniques* **35**(5), 39 (2024) <https://doi.org/10.1007/s41365-024-01407-3>
- [9] Ai, P., Wang, D., Huang, G., Sun, X.: Three-dimensional convolutional neural networks for neutrinoless double-beta decay signal/background discrimination in high-pressure gaseous Time Projection Chamber. *Journal of Instrumentation* **13**(08), 08015 (2018) <https://doi.org/10.1088/1748-0221/13/08/P08015>
- [10] Amaro, F.D., et al.: Bayesian network 3D event reconstruction in the Cygno optical TPC for dark matter direct detection. *The European Physical Journal C* **85**(11), 1261 (2025) <https://doi.org/10.1140/epjc/s10052-025-14965-6>
- [11] Ai, P., Wang, D., Sun, X., Huang, G., Li, Z.: A deep learning approach to multi-track location and orientation in gaseous drift chambers. *Nuclear Instruments and Methods in Physics Research Section A: Accelerators, Spectrometers, Detectors and Associated Equipment* **984**, 164640 (2020) <https://doi.org/10.1016/j.nima.2020.164640>
- [12] Jiao, Y., et al.: Optimization of deep learning method on track reconstruction for X-ray polarimetry with gas pixel detectors. *Experimental Astronomy* **59**(3), 34 (2025) <https://doi.org/10.1007/s10686-025-10003-1>
- [13] Detlefs, C., Rio, M., Mazzoli, C.: X-ray polarization: General formalism and polarization analysis. *The European Physical Journal Special Topics* **208**(1), 359–371 (2012) <https://doi.org/10.1140/epjst/e2012-01630-3>

- [14] Huang, X.-F., *et al.*: Simulation and photoelectron track reconstruction of soft X-ray polarimeter. *Nuclear Science and Techniques* **32**(7), 67 (2021) <https://doi.org/10.1007/s41365-021-00903-0>
- [15] Puetter, R.C., Yahil, A.: The pixon method of image reconstruction. *ASP Conf. Ser.* **172**, 307 (1999) [arXiv:astro-ph/9901063](https://arxiv.org/abs/astro-ph/9901063)
- [16] Panaretos, V.M., Zemel, Y.: Statistical Aspects of Wasserstein Distances. *Annual Review of Statistics and Its Application* **6**, 405–431 (2019) <https://doi.org/10.1146/annurev-statistics-030718-104938>
- [17] Kolouri, S., Rohde, G.K., Hoffmann, H.: Sliced Wasserstein Distance for Learning Gaussian Mixture Models. In: 2018 IEEE/CVF Conference on Computer Vision and Pattern Recognition, pp. 3427–3436 (2018). <https://doi.org/10.1109/CVPR.2018.00361>
- [18] Kolouri, S., Nadjahi, K., Simsekli, U., Badeau, R., Rohde, G.K.: Generalized Sliced Wasserstein Distances. In: *Advances in Neural Information Processing Systems 32: Annual Conference on Neural Information Processing Systems 2019, NeurIPS 2019, December 8-14, 2019, Vancouver, BC, Canada*, pp. 261–272 (2019)
- [19] Nietert, S., Goldfeld, Z., Sadhu, R., Kato, K.: Statistical, Robustness, and Computational Guarantees for Sliced Wasserstein Distances. In: *Advances in Neural Information Processing Systems 35: Annual Conference on Neural Information Processing Systems 2022, NeurIPS 2022, New Orleans, LA, USA, November 28 - December 9, 2022* (2022)
- [20] Deshpande, I., Zhang, Z., Schwing, A.: Generative Modeling Using the Sliced Wasserstein Distance. In: 2018 IEEE/CVF Conference on Computer Vision and Pattern Recognition, pp. 3483–3491 (2018). <https://doi.org/10.1109/CVPR.2018.00367>
- [21] Kitaguchi, T., *et al.*: A convolutional neural network approach for reconstructing polarization information of photoelectric X-ray polarimeters. *Nuclear Instruments and Methods in Physics Research Section A: Accelerators, Spectrometers, Detectors and Associated Equipment* **942**, 162389 (2019) <https://doi.org/10.1016/j.nima.2019.162389>
- [22] Li, Y.-N., *et al.*: Research on the X-ray polarization deconstruction method based on hexagonal convolutional neural network. *Nuclear Science and Techniques* **36**(2), 31 (2025) <https://doi.org/10.1007/s41365-024-01598-9>
- [23] Moriakov, N., Samudre, A., Negro, M., Gieseke, F., Otten, S., Hendriks, L.: Inferring astrophysical X-ray polarization with deep learning. *CoRR* **abs/2005.08126** (2020) [2005.08126](https://arxiv.org/abs/2005.08126)
- [24] Dort, K., Bilk, J., Käs, S., Lange, J.S., Peter, M., Schellhaas, T., Schwenker, B., Spruck, B.: Comparison of supervised and unsupervised anomaly detection in Belle II pixel detector data. *The European Physical Journal C* **82**(7), 587 (2022) <https://doi.org/10.1140/epjc/s10052-022-10548-x>
- [25] Hulsman, J.: POLAR-2: a large scale gamma-ray polarimeter for GRBs. In: *Space Telescopes and Instrumentation 2020: Ultraviolet to Gamma Ray*, vol. 11444, p. 114442 (2020). <https://doi.org/10.1117/12.2559374>
- [26] An, M., *et al.*: A low-noise CMOS pixel direct charge sensor, Topmetal-II. *Nuclear Instruments and Methods in Physics Research Section A: Accelerators, Spectrometers, Detectors and Associated Equipment* **810**, 144–150 (2016) <https://doi.org/10.1016/j.nima.2015.11.153>
- [27] Li, Z., *et al.*: Preliminary test of topmetal-II- sensor for X-ray polarization measurements. *Nuclear Instruments and Methods in Physics Research Section A: Accelerators, Spectrometers, Detectors and Associated Equipment* **1008**, 165430 (2021) <https://doi.org/10.1016/j.nima.2021.165430>
- [28] Gavrilin, M.: Relativistic  $K$ -Shell Photoeffect. *Phys. Rev.* **113**, 514–526 (1959) <https://doi.org/10.1103/PhysRev.113.514>

- [29] Xie, Y., *et al.*: Variably polarized X-ray sources for LPD calibration. *Experimental Astronomy* **56**(2), 499–515 (2023) <https://doi.org/10.1007/s10686-023-09905-9>
- [30] Li, Z., Liu, F., Yang, W., Peng, S., Zhou, J.: A Survey of Convolutional Neural Networks: Analysis, Applications, and Prospects. *IEEE Transactions on Neural Networks and Learning Systems* **33**(12), 6999–7019 (2022) <https://doi.org/10.1109/TNNLS.2021.3084827>
- [31] He, K., Zhang, X., Ren, S., Sun, J.: Delving Deep into Rectifiers: Surpassing Human-Level Performance on ImageNet Classification. In: 2015 IEEE International Conference on Computer Vision, ICCV 2015, Santiago, Chile, December 7–13, 2015, pp. 1026–1034 (2015). <https://doi.org/10.1109/ICCV.2015.123>
- [32] Paszke, A., *et al.*: PyTorch: An Imperative Style, High-Performance Deep Learning Library. In: *Advances in Neural Information Processing Systems 32: Annual Conference on Neural Information Processing Systems 2019, NeurIPS 2019, December 8–14, 2019, Vancouver, BC, Canada*, pp. 8024–8035 (2019)
- [33] Von Mises, R.: *Mathematical Theory of Probability and Statistics*. Academic press, New York and London (1964)
- [34] Hundrieser, S., Klatt, M., Munk, A.: In: Sen-Gupta, A., Arnold, B.C. (eds.) *The Statistics of Circular Optimal Transport*, pp. 57–82. Springer, Singapore (2022). [https://doi.org/10.1007/978-981-19-1044-9\\_4](https://doi.org/10.1007/978-981-19-1044-9_4)
- [35] Virtanen, P., *et al.*: SciPy 1.0: Fundamental Algorithms for Scientific Computing in Python. *Nature Methods* **17**, 261–272 (2020) <https://doi.org/10.1038/s41592-019-0686-2>
- [36] Flamary, R., *et al.*: POT: Python Optimal Transport. *Journal of Machine Learning Research* **22**(78), 1–8 (2021)
- [37] Erdmann, J., Graaf, A., Mausolf, F., Nackenhorst, O.: SR-GAN for SR-gamma: super resolution of photon calorimeter images at collider experiments. *The European Physical Journal C* **83**(11), 1001 (2023) <https://doi.org/10.1140/epjc/s10052-023-12178-3>
- [38] Fu, Z., Grant, C., Krawiec, D.M., Li, A., Winslow, L.A.: Generative models for simulation of KamLAND-Zen. *The European Physical Journal C* **84**(6), 651 (2024) <https://doi.org/10.1140/epjc/s10052-024-12980-7>